

A General Strategy to Immobilize Single-Atom Catalysts in Metal–Organic Frameworks for Enhanced Photocatalysis

Jianfei Sui, Hang Liu, Shaojin Hu, Kang Sun, Gang Wan, Hua Zhou, Xiao Zheng, and Hai-Long Jiang*

Single-atom catalysts (SACs) are witnessing rapid development due to their high activity and selectivity toward diverse reactions. However, it remains a grand challenge in the general synthesis of SACs, particularly featuring an identical chemical microenvironment and on the same support. Herein, a universal synthetic protocol is developed to immobilize SACs in metal–organic frameworks (MOFs). Significantly, by means of SnO₂ as a mediator or adaptor, not only different single-atom metal sites, such as Pt, Cu, and Ni, etc., can be installed, but also the MOF supports can be changed (for example, UiO-66-NH₂, PCN-222, and DUT-67) to afford M₁/SnO₂/MOF architecture. Taking UiO-66-NH₂ as a representative, the Pt₁/SnO₂/MOF exhibits approximately five times higher activity toward photocatalytic H₂ production than the corresponding Pt nanoparticles (≈2.5 nm) stabilized by SnO₂/UiO-66-NH₂. Remarkably, despite featuring identical parameters in the chemical microenvironment and support in M₁/SnO₂/UiO-66-NH₂, the Pt₁ catalyst possesses a hydrogen evolution rate of 2167 μmol g⁻¹ h⁻¹, superior to the Cu₁ and Ni₁ counterparts, which is attributed to the differentiated hydrogen binding free energies, as supported by density-functional theory (DFT) calculations. This is thought to be the first report on a universal approach toward the stabilization of SACs with identical chemical microenvironment on an identical support.

1. Introduction

Single-atom catalysts (SACs), being the ultimate size limit for metal nanoparticles (NPs) in supported catalysts, have captured intensive research interest.^[1] With maximized atomic utilization of metal catalysts and almost identical microenvironment, SACs show greatly enhanced activity and selectivity toward

diverse catalytic reactions, compared to the traditional metal NPs.^[2] However, the isolated single atoms are easy to migrate and sinter during reaction because of the high surface free energy, which remains a considerable challenge.^[3] In this context, many substrates, which might present strong coordination bonding and/or considerable charge transfer with isolated single atoms, are selected as the underlying supports of SACs, such as heteroatom-doped carbon materials,^[2a] metal oxides,^[2b,4] etc. Among diverse supports, metal oxides have been intensively investigated due to their abundant metal vacancies and surface OH groups to immobilize single atoms.^[1a,4] As an n-type semiconductor, SnO₂ is a widely adopted support for metal NPs as it usually provides high stability and strong interaction, the latter of which would improve the catalytic performance of metal sites.^[5] It is reported that the Sn²⁺ ion is capable of reducing noble metal ions in situ by oxidizing itself to SnO₂.^[6] Therefore, SnO₂ could also be


a suitable support for immobilizing SACs. Meanwhile, to fabricate SACs in reasonable loadings, the most straightforward and effective way is to adopt high-specific-area porous supports, which would enable the accessibility of well-dispersed metal sites.^[3a,b]

As a class of porous crystalline materials, metal–organic frameworks (MOFs),^[7] featuring very high surface area and high porosity, are recognized to be ideal candidates for stabilizing SACs. In fact, in reference to traditional inorganic supports, MOFs are able to provide abundant pore space and tailored microenvironment, which have been demonstrated to be excellent hosts/supports for metal NPs toward synergetic catalysis in recent years.^[8] Nevertheless, the current fabrication of SACs based on MOFs is mostly related to the pyrolysis of MOF precursors.^[1c,9] The facile construction of high-loading SACs by directly adopting MOFs has been rarely achieved.^[10] These reports are mostly based on two main approaches to MOF-supported SACs. One is to anchor SACs onto M–oxo clusters in MOFs, posing the prior request of the available chelating sites on the clusters, mainly Zr–oxo clusters.^[10a–d] The other way is to stabilize SACs by the adjacent coordination atoms in the organic linker.^[10e–g] There are respective requirements for particular MOF structures and components in these two strategies, which limit their synthetic universality. Therefore,

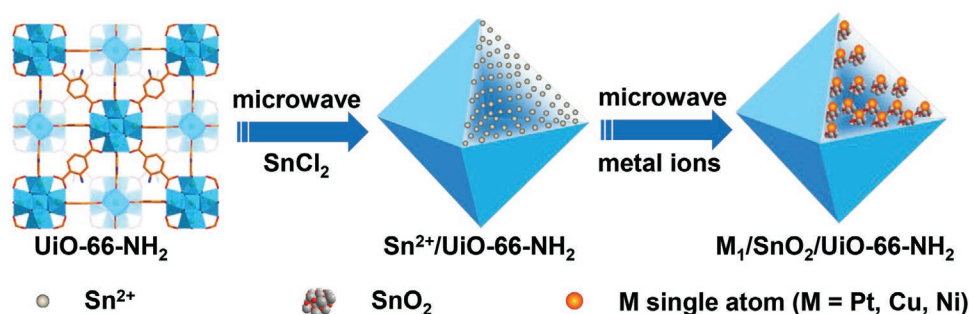
J. Sui, H. Liu, S. Hu, K. Sun, X. Zheng, H.-L. Jiang
College of Chemistry and Materials Science
University of Science and Technology of China
Hefei, Anhui 230026, P. R. China
E-mail: jianglab@ustc.edu.cn

G. Wan
Department of Mechanical Engineering and Department of Chemical Engineering
Stanford University
Stanford, CA 94305, USA

H. Zhou
X-ray Science Division
Advanced Photon Source Argonne National Laboratory
Lemont, IL 60439, USA

 The ORCID identification number(s) for the author(s) of this article can be found under <https://doi.org/10.1002/adma.202109203>.

DOI: 10.1002/adma.202109203



Scheme 1. Schematic illustration showing the microwave-assisted synthetic process for $M_1/SnO_2/MOF$, using UiO-66-NH₂ as a representative example.

the development of an alternative general strategy to fabricate SACs/MOF is highly desired.

In this work, we have integrated the advantages of SnO₂ and MOFs as supports and developed a general strategy for the immobilization of diverse SACs, such as Pt, Cu, and Ni, on SnO₂-furnished MOFs. Specifically, MOFs are first impregnated with Sn²⁺, followed by introducing the metal precursor under microwave-assisted conditions. In the subsequent step, the well-dispersed Sn²⁺ can proceed redox and hydrolysis reactions with introduced metal precursors, giving rise to the deposition of single metal atoms onto SnO₂ that is trapped in MOFs, denoted $M_1/SnO_2/MOF$ ($M = Pt, Cu, \text{ and } Ni$) (**Scheme 1**). Remarkably, the representative Pt₁/SnO₂/UiO-66-NH₂ exhibits an excellent activity in the visible-light photocatalytic H₂ production (2167 $\mu\text{mol g}^{-1} \text{ h}^{-1}$, TOF = 31 h^{-1}), among the highest H₂ production activity in reported MOF photocatalysis and approximately five times higher than its nanoparticle counterpart (denoted Pt_{NP}/SnO₂/UiO-66-NH₂). Density-functional theory (DFT) calculations reveal that the incorporation of single metal atoms greatly lowers the proton activation barrier, thereby accelerating the H₂ evolution.

2. Results and Discussion

2.1. Synthesis and Characterization

The UiO-66-NH₂ involving Zr₆O₄(OH)₄ clusters was synthesized by using ZrCl₄ and 2-aminoterephthalic acid (Figure S1, Supporting Information), with acetic acid as a modulator in DMF. The Sn²⁺ impregnated UiO-66-NH₂ (aliased as Sn²⁺/UiO-66-NH₂) was prepared by microwave-assisted reaction of SnCl₂·2H₂O and the MOF in acetonitrile. The loading amount of Sn²⁺ is 12.8 wt% detected by inductively coupled plasma atomic-emission spectrometry (ICP-AES). Powder X-ray diffraction (XRD) pattern indicates that the high crystallinity of UiO-66-NH₂ remains after modification (Figure S2, Supporting Information). Scanning electron microscopy (SEM) image shows that the octahedral shape of UiO-66-NH₂ keeps unchanged and no additional particles can be observed in the transmission electron microscopy (TEM) image (Figure S3, Supporting Information). The diffuse reflectance infrared Fourier transform (DRIFT) spectra show that the characteristic peaks of chelating sites (terminal –OH/–OH₂ and μ_3 -OH) on the Zr–oxo node at around 3673 and 2745 cm^{-1} essentially

weakened after incorporating Sn²⁺ ions (Figure S4, Supporting Information), indicating that Sn²⁺ ions have been successfully coordinated by the –OH/OH₂ groups terminating on the Zr–oxo clusters.^[10a,d]

The $M_1/SnO_2/UiO-66-NH_2$ were subsequently obtained by introducing metal precursors into Sn²⁺/UiO-66-NH₂ under microwave-assisted reaction. This strategy is powerful and general in the fabrication of diverse SACs, including Pt, Cu, Ni, etc. Taking Pt as an example, the Pt₁/SnO₂/UiO-66-NH₂ was prepared by microwave-assisted reaction of Sn²⁺/UiO-66-NH₂ with H₂PtCl₆ in acetonitrile. The loading amount of Pt is 1.35 wt% detected by ICP-AES. The high crystallinity of UiO-66-NH₂ can be well maintained after this modification, as indicated by powder XRD patterns (Figure S2, Supporting Information). The chemical stability investigations for Pt₁/SnO₂/UiO-66-NH₂ demonstrates the introduction of SnO₂ and Pt almost does not affect the stability of UiO-66-NH₂ (Figure S5, Supporting Information). Nitrogen sorption isotherms demonstrate that the MOF pore feature is maintained, while the adsorption capacity of Pt₁/SnO₂/UiO-66-NH₂ is slightly reduced due to the mass occupation of introduced components (Figure S6, Supporting Information). The UiO-66-NH₂ morphology is almost retained, which can be found in SEM and TEM images (Figure S7, Supporting Information). Close observation in high-resolution TEM (HRTEM) image suggests the particles in 1–2 nm with the lattice fringes and *d*-spacing of 0.34 and 0.26 nm can be observed (Figure S8, Supporting Information), which correspond to the (110) and (101) planes of tetragonal SnO₂ quantum dots,^[11] and their particles sizes can match the pore sizes of defective UiO-66.^[12] The chemical states of Pt, Sn, and Zr have been examined by X-ray photoelectron spectroscopy (XPS, Figure S9, Supporting Information). The peak of Zr 3d_{5/2} shifts to higher binding energy from 182.8 to 183.2 eV after modifying Sn²⁺ to UiO-66-NH₂, indicating the possible formation of Sn–O–Zr linkage. Accordingly, the peak at 487.3 eV for Sn 3d_{5/2} is assignable to Sn²⁺ in Sn²⁺/UiO-66-NH₂.^[13] After introducing Pt species in Sn²⁺-UiO-66-NH₂, these XPS peaks shift slightly to higher binding energies of 487.4 eV, which reasonably reflects the oxidation of Sn²⁺ to SnO₂ due to the spontaneous redox reaction between Sn²⁺ and PtCl₆²⁻ with suitable redox potentials and in accordance with the above HRTEM observation (Figure S8, Supporting Information),^[14] yielding Pt₁/SnO₂/UiO-66-NH₂. The binding energy of Pt 4f_{7/2} locates at 73.1 eV in Pt₁/SnO₂/UiO-66-NH₂, falling in the range between 71.2 and 74.2 eV, which verifies the Pt valence is between 0 and +2 (closer to +2).^[15]

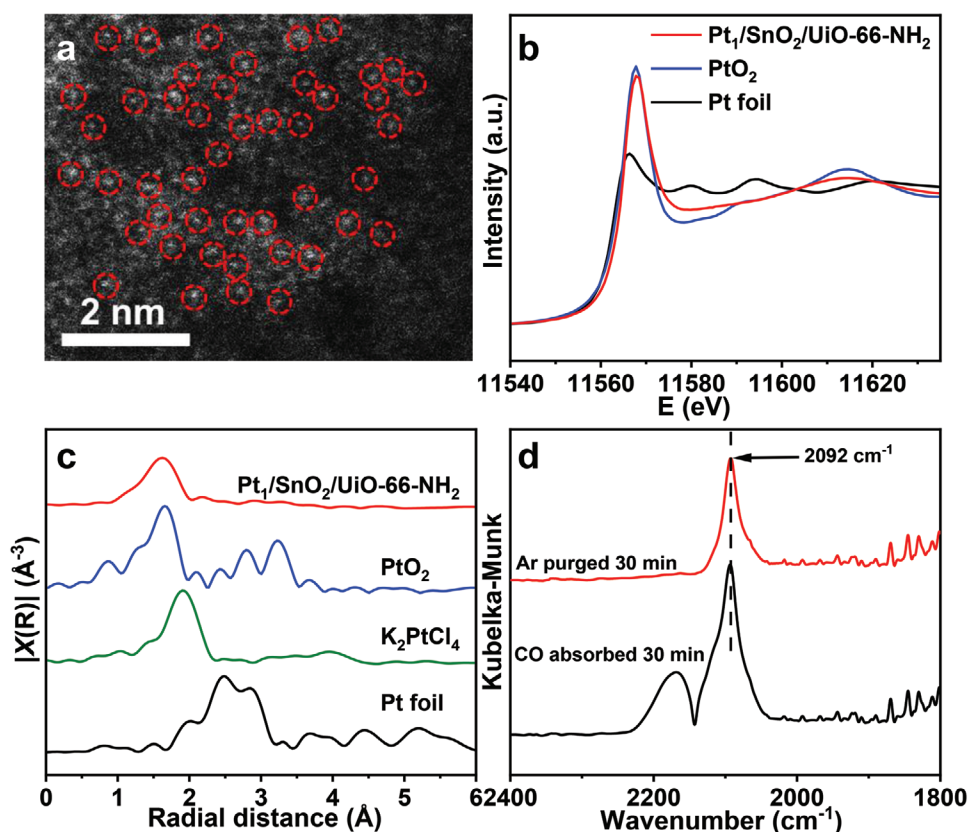


Figure 1. a) Aberration-corrected HAADF-STEM image of Pt₁/SnO₂/UiO-66-NH₂, in which single Pt atoms are highlighted by the red dashed circles. b) The Pt L₃-edge XANES spectra for Pt₁/SnO₂/UiO-66-NH₂, PtO₂, and Pt foil. c) Fourier transformed (FT) k^2 -weighted $\chi(k)$ -function of the EXAFS spectra for Pt₁/SnO₂/UiO-66-NH₂, PtO₂, K₂PtCl₄, and Pt foil. d) DRIFT spectra of CO adsorbed on Pt₁/SnO₂/UiO-66-NH₂ before and after purging with Ar gas for 30 min.

To investigate the microstructure of Pt species, high-angle annular dark-field scanning transmission electron microscopy (HAADF-STEM) observation was conducted. Single Pt atoms can be identified as bright spots in random distribution, as contrasted by other lighter elements, reflecting that Pt atoms are atomically dispersed while no Pt NPs are observable (Figure 1a). Given that electron microscope can provide the information of local structure only, X-ray absorption spectroscopy (XAS) was conducted to determine the coordination environment and chemical state of Pt species. In 5d transition metal L₃-edge, the peak intensity of X-ray absorption near-edge structure (XANES) is a good indicator of the number of unoccupied d-electron states.^[16] As shown in the Pt L₃-edge XANES profiles (Figure 1b), the peak intensity of Pt₁/SnO₂/UiO-66-NH₂ is significantly higher than that of Pt foil and closer to that of PtO₂, implying the existence of highly oxidized Pt states, which is in agreement with XPS results (Figure S9, Supporting Information). Fourier-transform extended X-ray absorption fine structure (FT-EXAFS) spectrum of Pt₁/SnO₂/UiO-66-NH₂ gives only a main peak at about 1.63 Å, which is assignable to the first shell of the Pt–O bond and no Pt–Cl bond at 1.90 Å (K₂PtCl₄) or Pt–Pt bond at 2.49 Å (Pt foil) can be found, demonstrating the generation of atomically dispersed Pt sites in Pt₁/SnO₂/UiO-66-NH₂ (Figure 1c). To further verify the Pt₁ coordination structure, EXAFS fitting has been performed. The best fitting

result for the first shell shows that each Pt atom is coordinated by about 4 oxygen atoms on average (Figure S10, inset, Table S1, Supporting Information). The overall EXAFS analysis on Pt–O₄ coordination around the atomically dispersed Pt ions is found to be consistent with the XANES observation of oxidized Pt species.

In addition, the carbon monoxide (CO) adsorption behavior in the DRIFT spectra provides another powerful evidence to determine the dispersion and oxidation state of Pt (Figure 1d). There is only one strong vibration band at 2092 cm⁻¹, ascribed to linearly chemisorbed CO on single Pt atoms, after purging with Ar for 30 min to evacuate gaseous CO. No observable peak in the range of 2080–2030 and 1920–1950 cm⁻¹ indicates the absence of linear- and bridged-adsorbed CO on the Pt clusters, reflecting no significant existence of Pt clusters and/or NPs in Pt₁/SnO₂/UiO-66-NH₂. Accordingly, most Pt species should be atomically dispersed, i.e., single-atomic Pt.^[15] Moreover, the location of CO adsorption peak is well retained after purging with Ar, which indicates that the dipole–dipole coupling interaction between adsorbed CO molecules on Pt does not exist, further supporting the isolation of Pt atoms.^[10e] The CO adsorption peak appears at 2092 cm⁻¹, a significant blue shift compared to the sharp peak at ≈2030 cm⁻¹ related to CO on Pt⁰, is ascribed to CO adsorbed on Pt^{δ+},^[15] in good agreement with the oxidation state results from the XAS and XPS spectra.

Interestingly, it is found the pre-introduction of Sn^{2+} in our synthetic process plays a crucial role in the subsequent formation of single Pt atoms. When UiO-66-NH₂ was directly treated with H_2PtCl_6 or a mixture of $\text{SnCl}_2 \cdot 2\text{H}_2\text{O}$ and H_2PtCl_6 by the same microwave-assisted modification (samples were named as Pt/UiO-66-NH₂ and Pt-SnO₂/UiO-66-NH₂, respectively), Pt NPs instead of SACs were obtained (Figures S11–S13, Supporting Information). To further explore the generality of our synthetic strategy to the immobilization of SACs in MOFs, Pt has been replaced by another two metals (Ni and Cu) to afford Ni₁/SnO₂/UiO-66-NH₂ and Cu₁/SnO₂/UiO-66-NH₂. The loading amounts of Ni²⁺ and Cu²⁺ are 0.42 and 0.14 wt%, respectively and the amount of Sn²⁺ remains to be ≈12 wt%. Similar to those observed for Pt₁/SnO₂/UiO-66-NH₂, the crystallinity of MOFs can be maintained after modification, as confirmed by powder XRD patterns (Figure S14, Supporting Information). SEM and TEM images indicate the morphologies of MOFs are almost intact and only small particles (about 1–2 nm) identified as SnO₂ are found (Figures S15–S17, Supporting Information). Nitrogen sorption isotherms indicate moderately reduced surface area after modification owing to the addition of Sn and Cu (or Ni) species (Figure S18, Supporting Information). Fortunately, we have indeed obtained their corresponding SACs by this synthetic strategy based on the XAS data. The Ni K-edge XANES spectrum of Ni₁/SnO₂/UiO-66-NH₂ indicates that the Ni₁ oxidation state falls into 0–+2 (closer to +2), which is in agreement with XPS results (Figure S19a,b, Supporting Information). The FT-EXAFS spectrum presents a dominated peak at ≈1.59 Å respecting to the Ni–O scattering path, and no Ni–Ni bond is detected (Figure S19c, Supporting Information). The six-fold coordinated O atoms in the first-shell of Ni₁ center in Ni₁/SnO₂/UiO-66-NH₂ have been resolved by the curve fitting for EXAFS data (Figure S19d, Table S1, Supporting Information). Similar results have been obtained and support the successful formation of single-atom Cu₁ with 4 coordinated oxygen atoms in Cu₁/SnO₂/UiO-66-NH₂ (Figure S20, Table S1, Supporting Information).

In addition to the alteration of single-atom metals, the generality of this synthetic strategy has been further demonstrated by replacing the MOF support, UiO-66-NH₂, with PCN-222 or DUT-67 (Figures S21 and S22, Supporting Information). All powder XRD patterns and SEM images display that the microstructure of these MOFs remains intact after modification (Figures S23 and S24, Supporting Information). The UV–vis diffuse reflectance spectra show that the incorporation of single atoms has no apparent influence on the intrinsic absorption of the MOFs (Figure S25, Supporting Information). Nitrogen sorption isotherms and pore size distributions for PCN-222 or DUT-67 demonstrate that their surface area and pore size present reasonable decrease after the introduction of SnO₂ and Pt species (Figures S26 and S27, Supporting Information). The XANES and EXAFS analyses unambiguously reveal the formation of atomically dispersed Pt species on diverse MOF supports mediated by SnO₂ (Figures S28 and S29, Supporting Information), similar to that in Pt₁/SnO₂/UiO-66-NH₂, affording Pt₁/SnO₂/PCN-222 and Pt₁/SnO₂/DUT-67.

2.2. Photoelectrochemical Properties

For comparison, Pt NPs (≈2.5 nm) stabilized by SnO₂/UiO-66-NH₂, namely Pt_{NP}/SnO₂/UiO-66-NH₂, were also synthesized

via a photochemical deposition process (Figures S30–S32, Supporting Information). UV–vis diffuse reflectance spectrum of UiO-66-NH₂ shows a strong absorption in ≈300–450 nm, which can be ascribed to the characteristic absorbance of ligand antenna (Figure 2a). The band structure of UiO-66-NH₂ calculated from Tauc plots and Mott–Schottky plots shows that it is thermodynamically possible for photocatalytic H₂ production (Figure S33, Supporting Information). The absorbance edge is almost identical after modification, which means that all the samples possess similar bandgaps. Photoluminescence (PL) emission spectra are collected under excitation at 385 nm, of which its fluorescent intensity can be an indicator of charge recombination (Figure 2b). As expected, the PL spectra show that the parent MOF has the strongest peak, followed by SnO₂/UiO-66-NH₂ and Pt_{NP}/SnO₂/UiO-66-NH₂ while Pt₁/SnO₂/UiO-66-NH₂ presents significant fluorescence extinction and the weakest fluorescence intensity, which can be explained as its best charge-separation efficiency. Reversed to the PL intensity, Pt₁/SnO₂/UiO-66-NH₂ displays the strongest photocurrent response among all investigated catalysts, suggesting the fastest interfacial charge transfer from UiO-66-NH₂ to Pt single-atoms under irradiation (Figure 2c). The above results are also supported by electrochemical impedance spectroscopy (EIS), where Pt₁/SnO₂/UiO-66-NH₂ possesses the smallest radius, indicative of the lowest charge transfer resistance between the catalyst and medium (Figure 2d).

The Cu- and Ni-based samples exhibit similar results to the Pt-based catalysts above. The Cu and Ni NPs were introduced to SnO₂/UiO-66-NH₂ via impregnation and reduced by NaBH₄ to give Cu_{NP}/SnO₂/UiO-66-NH₂ and Ni_{NP}/SnO₂/UiO-66-NH₂, respectively, for comparison (Figures S34 and S35, Supporting Information). The UV–vis diffuse reflectance, PL, photocurrent and EIS measurements for M₁/SnO₂/UiO-66-NH₂, M_{NP}/SnO₂/UiO-66-NH₂ (M = Cu and Ni) and SnO₂/UiO-66-NH₂ display exactly the same trends to the Pt-based samples (Figures S36–S39, Supporting Information). From these results, it is concluded that SACs possess the highest efficiency of charge transfer among all their corresponding counterparts. Further comparison of photoelectrochemical properties for all the three SACs samples, M₁/SnO₂/UiO-66-NH₂ (M = Pt, Cu, and Ni), demonstrates the superior efficiency of Pt₁/SnO₂/UiO-66-NH₂ to Cu₁/SnO₂/UiO-66-NH₂ and Ni₁/SnO₂/UiO-66-NH₂, toward charge separation (Figures S40–S43, Supporting Information).

2.3. Photocatalytic Activity

Encouraged by the above characterizations, we have then investigated catalytic performance of Pt₁/SnO₂/UiO-66-NH₂ for visible-light photocatalytic H₂ production by water splitting (Figure 3a). As expected, UiO-66-NH₂ shows a poor photocatalytic H₂ production rate of ≈18.7 μmol g⁻¹ h⁻¹, possibly attributed to the absence of overlap between the empty metal *d* orbital and/or the π* orbital of the organic linker and the obstructed electron transfer from the linker to metal.^[17] Upon loading Pt NPs, Pt_{NP}/SnO₂/UiO-66-NH₂ shows much enhanced activity of ≈423 μmol g⁻¹ h⁻¹, suggesting the critical role of Pt in photocatalysis. Strikingly, Pt₁/SnO₂/UiO-66-NH₂ achieves the highest photocatalytic H₂ production rate, 2167 μmol g⁻¹ h⁻¹ with the apparent quantum efficiency (AQE) of ≈2.23% at

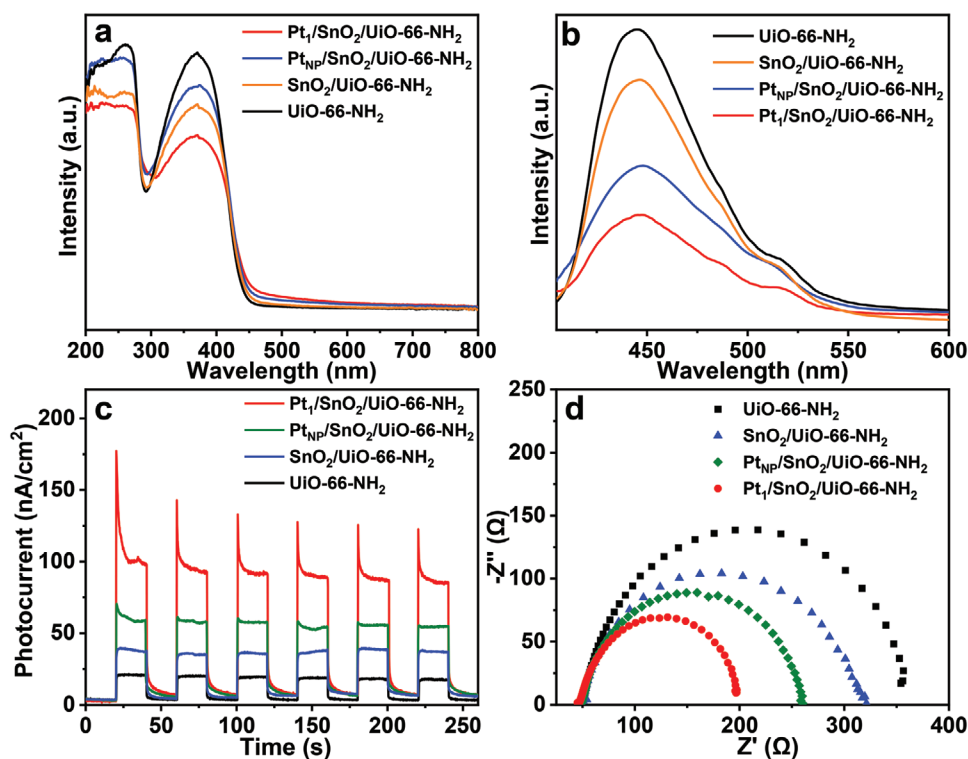


Figure 2. a) UV-vis spectra, b) PL emission spectra ($\lambda_{\text{exc}} = 385 \text{ nm}$), c) photocurrent responses, and d) EIS Nyquist plots for $\text{Pt}_1/\text{SnO}_2/\text{UiO-66-NH}_2$, $\text{Pt}_{\text{NP}}/\text{SnO}_2/\text{UiO-66-NH}_2$, $\text{SnO}_2/\text{UiO-66-NH}_2$, and UiO-66-NH_2 .

380 nm, among all investigated samples, which is ≈ 116 , 8, and 5 times higher than that of UiO-66-NH_2 , $\text{SnO}_2/\text{UiO-66-NH}_2$ and $\text{Pt}_{\text{NP}}/\text{SnO}_2/\text{UiO-66-NH}_2$, respectively, probably on account of maximum utilization of the Pt species. Photocatalytic results show that, irrespective of the metals, the $\text{M}_1/\text{SnO}_2/\text{UiO-66-NH}_2$ exhibit much higher hydrogen production rate than $\text{M}_{\text{NP}}/\text{SnO}_2/\text{UiO-66-NH}_2$ and other counterparts (Figure S44, Supporting Information), demonstrating that single-atom metal dramatically boosts the photocatalytic activity. Furthermore, $\text{Pt}_1/\text{SnO}_2/\text{UiO-66-NH}_2$ outperforms the other $\text{M}_1/\text{SnO}_2/\text{UiO-66-NH}_2$ ($\text{M} = \text{Cu}$ and Ni) and displays the highest activity (Figure 3a).

It is believed that the Pt behaves as a cocatalyst to trap electrons for hydrogen evolution; its low overpotential is responsible for the high performance. The recycling experiments indicate no noticeable activity drop occurs to all $\text{M}_1/\text{SnO}_2/\text{UiO-66-NH}_2$ (Figure 3b; Figure S45, Supporting Information). Powder XRD patterns, SEM, TEM, and HRTEM images confirm that the MOF crystallinity and structural integrity are well maintained and no Pt NPs can be found after reaction (Figures S46 and S47, Supporting Information). The atomically dispersed status of catalytic metal centers in these catalysts is also verified by EXAFS and CO adsorption behavior in the DRIFT spectra for

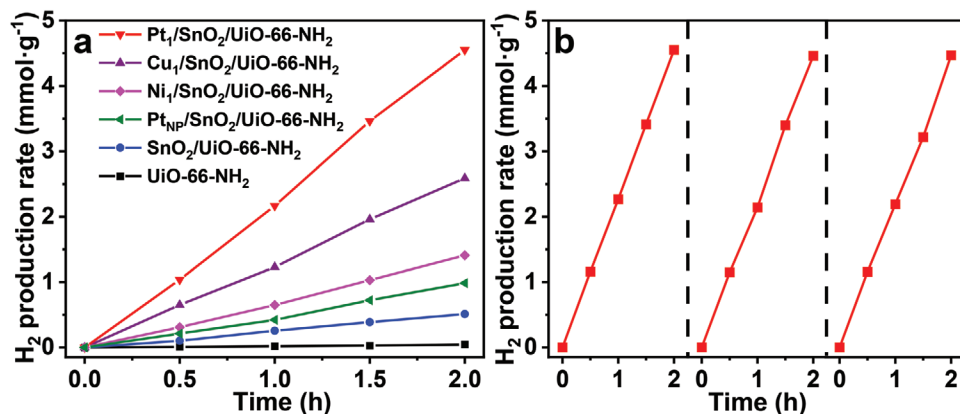


Figure 3. a) Photocatalytic hydrogen production rates for $\text{Pt}_1/\text{SnO}_2/\text{UiO-66-NH}_2$, $\text{Cu}_1/\text{SnO}_2/\text{UiO-66-NH}_2$, $\text{Ni}_1/\text{SnO}_2/\text{UiO-66-NH}_2$, $\text{Pt}_{\text{NP}}/\text{SnO}_2/\text{UiO-66-NH}_2$, $\text{SnO}_2/\text{UiO-66-NH}_2$, and UiO-66-NH_2 . b) Performance in three consecutive runs of photocatalytic recycling for $\text{Pt}_1/\text{SnO}_2/\text{UiO-66-NH}_2$.

$M_1/SnO_2/UiO-66-NH_2$ after reaction (Figures S48 and S49, Supporting Information). These results highlight the good stability of $M_1/SnO_2/UiO-66-NH_2$ in the photocatalytic process.

Electron paramagnetic resonance (EPR) was conducted to illustrate the charge transfer and further reveal the mechanism in the photocatalytic process (Figure S50, Supporting Information). The EPR spectrum of $Pt_1/SnO_2/UiO-66-NH_2$ gives signals at g values of 2.001, 2.006, and 2.029 upon visible-light irradiation for 60 s in the solvent of acetonitrile with triethylamine as a sacrificial agent. The three EPR signals can be attributed to $O_2^{\cdot-}$ trapped in Zr-oxo clusters, while the g value of 2.001 may overlap with the signal of oxygen vacancies.^[18] It is assumed that the adsorbed O_2 molecules accept electrons from electron-trapped Zr-oxo clusters based on the ligand-to-cluster charge transfer (LCCT) process. Inspired by the above results, the overall reaction mechanism of $Pt_1/SnO_2/UiO-66-NH_2$ involved in the system can be proposed: (1) the electron-hole pairs are generated from the photoexcited amino functionalized organic linker (antenna) under visible light irradiation; (2) electrons are transferred to Zr-oxo clusters via LCCT process; and (3) electrons further migrate to the single Pt atoms for subsequent proton reduction.^[17b,19] Remarkably, $Pt_1/SnO_2/UiO-66-NH_2$ gives stronger EPR signals than $Pt_{NP}/SnO_2/UiO-66-NH_2$, $SnO_2/UiO-66-NH_2$, and $UiO-66-NH_2$, which could be attributed to the greatly accelerated electron transfer in the optimized SACs. Furthermore, the strongest EPR signals of $Pt_1/SnO_2/UiO-66-NH_2$ among all investigated SACs is in well line with its superior catalytic performance (Figure S50, Supporting Information).

According to the above experimental results, the activity of photocatalytic H_2 production can be significantly improved with SACs. DFT calculations were carried out to figure out the role of SACs in $Pt_1/SnO_2/UiO-66-NH_2$ (Figure 4a; Section S3

and Table S2, Supporting Information). The Gibbs free energy (ΔG_{H^*}) represents the free energy barrier of proton reduction, a key step of photocatalytic H_2 production; the absolute value approaching to 0 eV is favorable to the H_2 production activity of the photocatalyst. The $Pt_1/SnO_2/UiO-66-NH_2$ is able to significantly reduce the ΔG_{H^*} to -0.28 eV (Figure 4b). The extremely low value of ΔG_{H^*} would not only expedite electron-proton acceptance to form H^* , but also guarantee the fast hydrogen desorption. The ΔG_{H^*} value of $Pt_{NP}/SnO_2/UiO-66-NH_2$ is calculated to be -0.50 eV, which means that its overall free energy barrier is higher than that in $Pt_1/SnO_2/UiO-66-NH_2$ (Figure 4c). Therefore, the single Pt atoms not only maximize the Pt utilization but also feature extremely low absolute value of ΔG_{H^*} to facilitate hydrogen generation. In comparison, the ΔG_{H^*} values of $Cu_1/SnO_2/UiO-66-NH_2$ and $Ni_1/SnO_2/UiO-66-NH_2$ are calculated to be 0.39 and 0.46 eV, respectively, slightly higher than that of $Pt_1/SnO_2/UiO-66-NH_2$, which is consistent with experimental catalytic results and further illustrates the higher activity of the latter. Given the identical chemical microenvironment and support, the fabrication of $M_1/SnO_2/UiO-66-NH_2$ indeed provides an ideal SAC platform to differentiate the intrinsic activity of diverse single-atom metal species.

3. Conclusion

We have developed a general, two-step approach toward the immobilization of single-atom metal sites ($M = Pt, Cu, \text{ and } Ni$) in diverse MOFs ($UiO-66-NH_2$, PCN-222 and DUT-67), by supporting SnO_2 as a mediator/adaptor onto metal-oxo clusters via microwave-assisted modification. The SnO_2 offers strong interaction to stabilize the SACs, and the high surface area and high porosity of MOFs extend the dispersion distance of metal

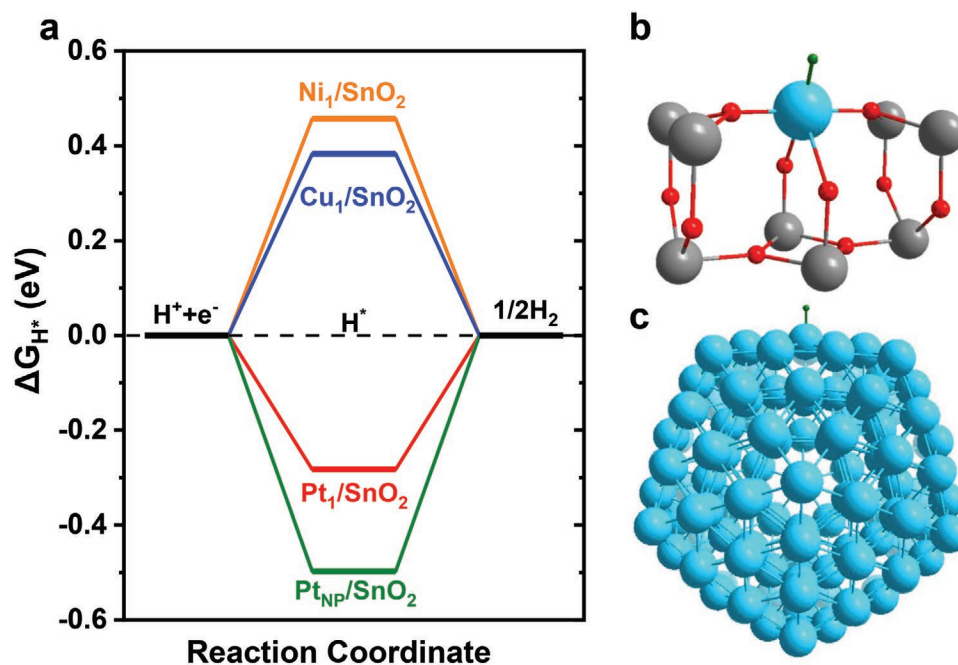


Figure 4. a) Calculated free energy diagram of catalyst loaded to $UiO-66-NH_2$ for photocatalytic H_2 production. b, c) Geometric structures of H^* of Pt_1/SnO_2 in $Pt_1/SnO_2/UiO-66-NH_2$ (b) and Pt NPs (c). The cyan, gray, red, and green balls represent Pt, Sn, O, and H atoms, respectively.

atoms and guarantees their accessibility in catalysis. Particularly, thanks to the maximum utilization of metal atoms, the atomically dispersed Pt in Pt₁/SnO₂/UiO-66-NH₂ displays the best photocatalytic hydrogen activity up to 2167 μmol g⁻¹ h⁻¹, superior to that of Cu₁/SnO₂/UiO-66-NH₂ (1265 μmol g⁻¹ h⁻¹) and Ni₁/SnO₂/UiO-66-NH₂ (654 μmol g⁻¹ h⁻¹), and far outperforming their corresponding metal NPs and other counterparts. DFT calculations reveal that the single Pt atoms possess a lower absolute value of hydrogen binding energy than both Pt NPs and single Cu/Ni atoms, accounting for the best photocatalytic hydrogen production activity of single Pt atoms. This study not only highlights the great potential and opportunities in the general fabrication of SACs in MOF systems, but also provides significant insight into the catalytic mechanism toward photocatalytic hydrogen production over single metal atoms.

Supporting Information

Supporting Information is available from the Wiley Online Library or from the author.

Acknowledgements

This work was supported by the National Key Research and Development Program of China (2021YFA1500400), the National Natural Science Foundation of China (21725101, 22161142001, 21521001), the DNL Cooperation Fund, Chinese Academy of Sciences (DNL201911), Collaborative Innovation Program of Hefei Science Center, CAS (2020HSC-CIP005), and the Fundamental Research Funds for the Central Universities (WK3450000007). This research used resources of the Advanced Photon Source, an Office of Science User Facility operated for the U.S. Department of Energy (DOE) Office of Science by Argonne National Laboratory and was supported by the U.S. DOE under Contract No. DE-AC02-06CH11357. The authors acknowledge the XAS supports from BSRF and SSRF. The calculations in this work are supported by the Supercomputing Center of USTC.

Conflict of Interest

The authors declare no conflict of interest.

Data Availability Statement

The data that support the findings of this study are available from the corresponding author upon reasonable request.

Keywords

H₂ production, metal–organic frameworks, photocatalysis, single-atom catalysts

Received: November 14, 2021

Revised: December 7, 2021

Published online: December 23, 2021

[1] a) A. Wang, J. Li, T. Zhang, *Nat. Rev. Chem.* **2018**, *2*, 65; b) L. Liu, A. Corma, *Chem. Rev.* **2018**, *118*, 4981; c) L. Jiao, H.-L. Jiang, *Chem*

- 2019**, *5*, 786; d) Y.-S. Wei, M. Zhang, R. Zou, Q. Xu, *Chem. Rev.* **2020**, *120*, 12089; e) J. Yang, W. Li, D. Wang, Y. Li, *Small Struct.* **2021**, *2*, 2000051.
- [2] a) P. Liu, Y. Zhao, R. Qin, S. Mo, G. Chen, L. Gu, D. M. Chevrier, P. Zhang, Q. Guo, D. Zang, B. Wu, G. Fu, N. Zheng, *Science* **2016**, *352*, 797; b) S. Ji, Y. Chen, X. Wang, Z. Zhang, D. Wang, Y. Li, *Chem. Rev.* **2020**, *21*, 11900; c) Y. Wang, J. Mao, X. Meng, L. Yu, D. Deng, X. Bao, *Chem. Rev.* **2019**, *119*, 1806; d) C. Zhu, Q. Shi, S. Feng, D. Du, Y. Lin, *ACS Energy Lett.* **2018**, *3*, 1713; e) X. Li, X. Yang, Y. Huang, T. Zhang, B. Liu, *Adv. Mater.* **2019**, *31*, 1902031; f) H. Zhang, G. Liu, L. Shi, J. Ye, *Adv. Energy Mater.* **2018**, *8*, 1701343; g) C. Tang, L. Chen, H. Li, L. Li, Y. Jiao, Y. Zheng, H. Xu, K. Davey, S.-Z. Qiao, *J. Am. Chem. Soc.* **2021**, *143*, 7819.
- [3] a) J. Liu, *ACS Catal.* **2017**, *7*, 34; b) L. Jiao, R. Zhang, G. Wan, W. Yang, X. Wan, H. Zhou, J. Shui, S.-H. Yu, H.-L. Jiang, *Nat. Commun.* **2020**, *11*, 2831; c) L. Lin, W. Zhou, R. Gao, S. Yao, X. Zhang, W. Xu, S. Zheng, Z. Jiang, Q. Yu, Y.-W. Li, C. Shi, X.-D. Wen, D. Ma, *Nature* **2017**, *544*, 80; d) P. Zhou, H. Chen, Y. Chao, Q. Zhang, W. Zhang, F. Lv, L. Gu, Q. Zhao, N. Wang, J. Wang, S. Guo, *Nat. Commun.* **2021**, *12*, 4412; e) X. Rong, H.-J. Wang, X.-L. Lu, R. Si, T.-B. Lu, *Angew. Chem., Int. Ed.* **2020**, *59*, 1961.
- [4] a) L. DeRita, S. Dai, K. Lopez-Zepeda, N. Pham, G. W. Graham, X. Pan, P. Christopher, *J. Am. Chem. Soc.* **2017**, *139*, 14150; b) L. Nie, D. Mei, H. Xiong, B. Peng, Z. Ren, X. I. P. Hernandez, A. DeLaRiva, M. Wang, M. H. Engelhard, L. Kovarik, A. K. Datye, Y. Wang, *Science* **2017**, *358*, 1419; c) Z. Jakub, J. Hulva, M. Meier, R. Bliem, F. Kraushofer, M. Setvin, M. Schmid, U. Diebold, C. Franchini, G. S. Parkinson, *Angew. Chem., Int. Ed.* **2019**, *58*, 13961.
- [5] a) W. Zhang, Q. Qin, L. Dai, R. Qin, X. Zhao, X. Chen, D. Ou, J. Chen, T. T. Chuong, B. Wu, N. Zheng, *Angew. Chem., Int. Ed.* **2018**, *57*, 9475; b) D.-J. Yang, I. Karnienchick, D. Y. Youn, A. Rothschild, I.-D. Kim, *Adv. Funct. Mater.* **2010**, *20*, 4258; c) B. Shen, L. Huang, J. Shen, L. Meng, E. J. Kluender, C. Wolverton, B. Tian, C. A. Mirkin, *J. Am. Chem. Soc.* **2020**, *142*, 18324.
- [6] a) Z. Yan, L. Fu, X. Zuo, H. Yang, *Appl. Catal., B* **2018**, *226*, 23; b) A. Sankar, K. Gunasekera, Z. Nan, A. Welton, J. Fang, K. Tonniss, R. Terrell, P. Boolchand, A. P. Angelopoulos, *J. Mater. Chem. A* **2020**, *8*, 17634; c) L. S. Zhong, J. S. Hu, Z. M. Cui, L. J. Wan, W. G. Song, *Chem. Mater.* **2007**, *19*, 4557.
- [7] a) H.-C. Zhou, S. Kitagawa, *Chem. Soc. Rev.* **2014**, *43*, 5415; b) H. Furukawa, K. E. Cordova, M. O’Keeffe, O. M. Yaghi, *Science* **2013**, *341*, 1230444; c) T. Islamoglu, S. Goswami, Z. Li, A. J. Howarth, O. K. Farha, J. T. Hupp, *Acc. Chem. Res.* **2017**, *50*, 805; d) B. Li, H.-M. Wen, Y. Cui, W. Zhou, G. Qian, B. Chen, *Adv. Mater.* **2016**, *28*, 8819; e) L. Jiao, J. Wang, H.-L. Jiang, *Acc. Mater. Res.* **2021**, *2*, 327; f) S. S. A. Shah, T. Najam, M. Wen, S.-Q. Zang, A. Waseem, H.-L. Jiang, *Small Struct.*, <https://doi.org/10.1002/sstr.202100090>; g) J. Nyakuchena, S. Ostresh, D. Streater, B. Pattengale, J. Neu, C. Fiankor, W. Hu, E. D. Kingstein, J. Zhang, X. Zhang, C. A. Schmuttenmaer, J. Huang, *J. Am. Chem. Soc.* **2020**, *142*, 21050.
- [8] a) Q. Yang, Q. Xu, H.-L. Jiang, *Chem. Soc. Rev.* **2017**, *46*, 4774; b) L. Chen, Q. Xu, *Matter* **2019**, *1*, 57; c) G. Lu, S. Li, Z. Guo, O. K. Farha, B. G. Hauser, X. Qi, Y. Wang, X. Wang, S. Han, X. Liu, J. S. DuChene, H. Zhang, Q. Zhang, X. Chen, J. Ma, S. C. J. Loo, W. D. Wei, Y. Yang, J. T. Hupp, F. Huo, *Nat. Chem.* **2012**, *4*, 310; d) Y. Wu, J. Shi, S. Mei, H. A. Katimba, Y. Sun, X. Wang, K. Liang, Z. Jiang, *ACS Catal.* **2020**, *10*, 9664; e) Y. C. Tan, H. C. Zeng, *Nat. Commun.* **2018**, *9*, 4326; f) L. Qi, J. Chen, B. Zhang, R. Nie, Z. Qi, T. Kobayashi, Z. Bao, Q. Yang, Q. Ren, Q. Sun, Z. Zhang, W. Huang, *ACS Catal.* **2020**, *10*, 5707; g) M. Zhao, K. Yuan, Y. Wang, G. Li, J. Guo, L. Gu, W. Hu, H. Zhao, Z. Tang, *Nature* **2016**, *539*, 76; h) K. M. Choi, D. Kim, B. Rungtaweeworanit, C. A. Trickett, J. T. D. Barmanbek, A. Alshammari, P. Yang, O. M. Yaghi, *J. Am. Chem. Soc.* **2017**, *139*, 356; i) H. Kobayashi, J. M. Taylor, Y. Mitsuoka, N. Ogiwara, T. Yamamoto, T. Toriyama, S. Matsumura, H. Kitagawa,

- Chem. Sci.* **2019**, *10*, 3289; j) G. Li, S. Zhao, Y. Zhang, Z. Tang, *Adv. Mater.* **2018**, *30*, 1800702.
- [9] a) S. Dang, Q.-L. Zhu, Q. Xu, *Nat. Rev. Mater.* **2017**, *3*, 17075; b) Y.-Z. Chen, R. Zhang, L. Jiao, H.-L. Jiang, *Coord. Chem. Rev.* **2018**, *362*, 1; c) Y. Chen, S. Ji, C. Chen, Q. Peng, D. Wang, Y. Li, *Joule* **2018**, *2*, 1242; d) H. Huang, K. Shen, F. Chen, Y. Li, *ACS Catal.* **2020**, *10*, 6579.
- [10] a) A. M. Abdel-Mageed, B. Rungtaweivoranit, M. Parlinska-Wojtan, X. Pei, O. M. Yaghi, R. J. Behm, *J. Am. Chem. Soc.* **2019**, *141*, 5201; b) B. An, J. Zhang, K. Cheng, P. Ji, C. Wang, W. Lin, *J. Am. Chem. Soc.* **2017**, *139*, 3834; c) K.-i. Otake, Y. Cui, C. T. Buru, Z. Li, J. T. Hupp, O. K. Farha, *J. Am. Chem. Soc.* **2018**, *140*, 8652; d) X. Ma, H. Liu, W. Yang, G. Mao, L. Zheng, H.-L. Jiang, *J. Am. Chem. Soc.* **2021**, *143*, 12220; e) X. Fang, Q. Shang, Y. Wang, L. Jiao, T. Yao, Y. Li, Q. Zhang, Y. Luo, H.-L. Jiang, *Adv. Mater.* **2018**, *30*, 1705112; f) H. Zhang, J. Wei, J. Dong, G. Liu, L. Shi, P. An, G. Zhao, J. Kong, X. Wang, X. Meng, J. Zhang, J. Ye, *Angew. Chem., Int. Ed.* **2016**, *55*, 14310; g) Q. Zuo, T. Liu, C. Chen, Y. Ji, X. Gong, Y. Mai, Y. Zhou, *Angew. Chem., Int. Ed.* **2019**, *58*, 10198; h) X. Wang, W. Chen, L. Zhang, T. Yao, W. Liu, Y. Lin, H. Ju, J. Dong, L. Zheng, W. Yan, X. Zheng, Z. Li, X. Wang, J. Yang, D. He, Y. Wang, Z. Deng, Y. Wu, Y. Li, *J. Am. Chem. Soc.* **2017**, *139*, 9419; i) J. Zhang, T. Bai, H. Huang, M.-H. Yu, X. Fan, Z. Chang, X.-H. Bu, *Adv. Mater.* **2020**, *32*, 2004747; j) J. He, N. Li, Z.-G. Li, M. Zhong, Z.-X. Fu, M. Liu, J.-C. Yin, Z. Shen, W. Li, J. Zhang, Z. Chang, X.-H. Bu, *Adv. Funct. Mater.* **2021**, *31*, 2103597.
- [11] a) K. Nagasawa, S. Takao, S.-i. Nagamatsu, G. Samjeské, O. Sekizawa, T. Kaneko, K. Higashi, T. Yamamoto, T. Uruga, Y. Iwasawa, *J. Am. Chem. Soc.* **2015**, *137*, 12856; b) Z. Li, R. Wang, J. Xue, X. Xing, C. Yu, T. Huang, J. Chu, K.-L. Wang, C. Dong, Z. Wei, Y. Zhao, Z.-K. Wang, Y. Yang, *J. Am. Chem. Soc.* **2019**, *141*, 17610.
- [12] a) F. Ahmadijokani, R. Mohammadkhani, S. Ahmadipouya, A. Shokrgozar, M. Rezakazemi, H. Molavi, T. M. Aminabhavi, M. Arjmand, *Chem. Eng. J.* **2020**, *399*, 125346; b) Y. Jiao, Y. Liu, G. Zhu, J. T. Hungerford, S. Bhattacharyya, R. P. Lively, D. S. Sholl, K. S. Walton, *J. Phys. Chem. C* **2017**, *121*, 23471.
- [13] a) T. Li, C. Yang, J.-L. Luo, G. Zheng, *ACS Catal.* **2019**, *9*, 10440; b) L. Romani, A. Speltini, F. Ambrosio, E. Mosconi, A. Profumo, M. Marelli, S. Margadonna, A. Milella, F. Fracassi, A. Listorti, F. D. Angelis, L. Malavasi, *Angew. Chem., Int. Ed.* **2021**, *60*, 3611.
- [14] a) X. Shen, T. Nagai, F. Yang, L.-Q. Zhou, Y. Pan, L. Yao, D. Wu, Y.-S. Liu, J. Feng, J. Guo, H. Jia, Z. Peng, *J. Am. Chem. Soc.* **2019**, *141*, 9463; b) V. Tallapally, R. J. A. Esteves, L. Nahar, I. U. Arachchige, *Chem. Mater.* **2016**, *28*, 5406.
- [15] B. Qiao, A. Wang, X. Yang, L. F. Allard, Z. Jiang, Y. Cui, J. Liu, J. Li, T. Zhang, *Nat. Chem.* **2011**, *3*, 634.
- [16] a) J. P. Clancy, N. Chen, C. Y. Kim, W. F. Chen, K. W. Plumb, B. C. Jeon, T. W. Noh, Y.-J. Kim, *Phys. Rev. B* **2012**, *86*, 195131; b) D. H. Pearson, C. C. Ahn, B. Fultz, *Phys. Rev. B* **1993**, *47*, 8471; c) G. Wan, J. W. Freeland, J. Kloppenburg, G. Petretto, J. N. Nelson, D.-Y. Kuo, C.-J. Sun, J. Wen, J. T. Diulus, G. S. Herman, Y. Dong, R. Kou, J. Sun, S. Chen, K. M. Shen, D. G. Schlom, G.-M. Rignanese, G. Hautier, D. D. Fong, Z. Feng, H. Zhou, J. Suntivich, *Sci. Adv.* **2021**, *7*, eabc7323.
- [17] a) M. A. Nasalevich, C. H. Hendon, J. G. Santaclara, K. Svane, B. van der Linden, S. L. Veber, M. V. Fedin, A. J. Houtepen, M. A. van der Veen, F. Kapteijn, A. Walsh, J. Gascon, *Sci. Rep.* **2016**, *6*, 23676; b) X. Ma, L. Wang, Q. Zhang, H.-L. Jiang, *Angew. Chem., Int. Ed.* **2019**, *58*, 12175.
- [18] a) C. Xu, Y. Pan, G. Wan, H. Liu, L. Wang, H. Zhou, S.-H. Yu, H.-L. Jiang, *J. Am. Chem. Soc.* **2019**, *141*, 19110; b) J. Long, S. Wang, Z. D. , S. Wang, Y. Zhou, L. Huang, X. Wang, *Chem. Commun.* **2012**, *48*, 11656.
- [19] a) J.-D. Xiao, Q. Shang, Y. Xiong, Q. Zhang, Y. Luo, S.-H. Yu, H.-L. Jiang, *Angew. Chem., Int. Ed.* **2016**, *55*, 9389; b) D. Sun, Y. Fu, W. Liu, L. Ye, D. Wang, L. Yang, X. Fu, Z. Li, *Chem. - Eur. J.* **2013**, *19*, 14279.